ACS Macro Letters

Letter

pubs.acs.org/macroletters

Understanding Water Uptake and Transport in Nafion Using X-ray Microtomography

Gi Suk Hwang,[†] Dilworth Y. Parkinson,[‡] Ahmet Kusoglu,[†] Alastair A. MacDowell,[‡] and Adam Z. Weber*[,†]

[†]Environmental Energy Technologies Division and [‡]Advanced Light Source, Lawrence Berkeley National Laboratory, 1 Cyclotron Road, Berkeley, California, 94720, United States

Supporting Information

ABSTRACT: To develop new ionomers and optimize existing ones, there is a need to understand their structure/function relationships experimentally. In this letter, synchrotron X-ray microtomography is used to examine water distributions within Nafion, the most commonly used ionomer. Simultaneous high spatial (~1 μm) and temporal (~10 min) resolutions, previously unattained by other techniques, clearly show the nonlinear water profile across the membrane thickness, with a continuous transition from dynamic to steady-state transport coefficients with the requisite water-content dependence. The data also demonstrate the importance of the interfacial condition in controlling the water profile and help to answer some long-standing debates in the literature.

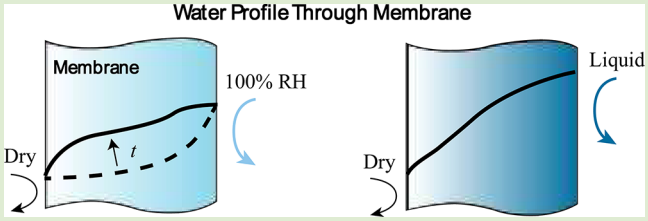

The canonical ion-conducting polymer for various electrochemical technologies is Nafion,[1−5] a member of a class of perfluorinated sulfonic-acid ionomers exhibiting outstanding ion conductivity and high chemical/mechanical stability once hydrated.[3,6,7] Although Nafion has been widely studied, significant knowledge gaps remain, where dynamic or even steady-state water-transport occurs.[8] To elucidate the fundamentals, water distributions within the membrane need to be visualized, which has been limited by spatial and temporal resolutions.[9] Herein, synchrotron-based X-ray microtomography is adapted to determine the water profiles with high resolution (~1 μm, ~10 min).

Nafion consists of a hydrophobic polytetrafluoroethylene backbone functionalized with hydrophilic sulfonic-acid-terminated side chains (Figure S1). Upon hydration, the hydrophobic and hydrophilic moieties nanophase separate and form a well-interconnected, water-domain network within the hydrophobic matrix. While it is known that Nafion's properties are highly water-content dependent, there are numerous conflicting measurements and conclusions reported, such as water-transport properties that vary widely, that is, ~10^{-10} to 10^{-6} cm^2/s.[8] The exact transport mechanisms still remain under contention with unresolved issues including whether diffusivity is water-content dependent[10] or independent,[11] whether diffusion is Fickian[11−13] or non-Fickian,[14−16] and whether the transport coefficient increases or decreases with increasing water content. In addition, it is known that Nafion's water uptake differs from vapor- and liquid-saturated reservoirs, that is, λ = 14 versus 22 at 25 °C[10] (λ is the water content, the number of water molecules per sulfonic-acid group, see Supporting Information), which is known as Schröder's paradox.[17] Although the exact origin is still under debate,[18,19] further examination is necessary for fundamental understanding of polymer physics as well as the practical applications because vapor and liquid boundaries often exist in operation (e.g., fuel cells).

To settle these conflicts, the water profile in the membrane is required. This has been performed to a certain extent (see Supporting Information),[20] but the techniques employed all suffered from either low spatial resolution (~5 to 50 μm) compared to the typical membrane thickness of 10 to 200 μm, limited experimental conditions, or long temporal resolution (~1 h for the higher spatial resolutions).

To meet the required spatial and temporal resolution targets, synchrotron-based, attenuation-contrast, X-ray computed microtomography, a technique typically reserved for structure and phase identification in hard materials, is employed. This technique, including modifications to overcome signal-to-noise sensitivity issues (as described in Supporting Information), is used for one of the first times to study dynamic and steady-state water profiles in soft matter with micrometer spatial and minute temporal resolutions under different water boundary conditions.[21,22] A typical image and developed sample holder are shown in Figures S2 and S3d, respectively.

For validation and calibration, the technique was used to examine membranes of known water content, that is, dry, vapor-saturated (VS), and liquid-saturated (LS) Nafion. Figure 1a shows the sample raw data from the X-ray tomography (corresponding to degree of attenuation per voxel, β and ρ are the mass attenuation coefficient and density of the material,

Received: December 18, 2012
Accepted: March 14, 2013
Published: March 18, 2013

   dx.doi.org/10.1021/mz300651a | *ACS Macro Lett.* 2013, 2, 288−291

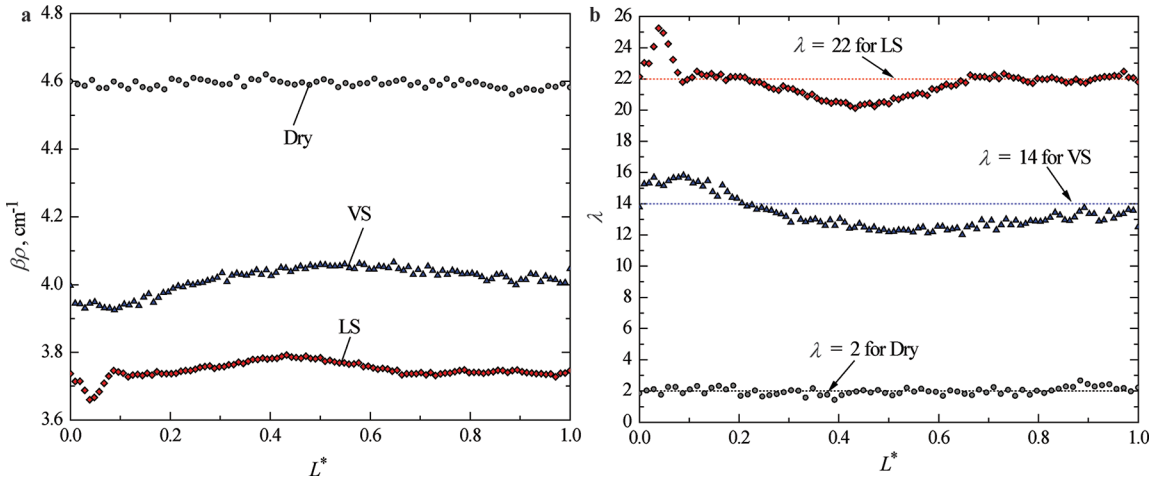

Figure 1. (a) Measured X-ray attenuation coefficients for dry, vapor-saturated (VS), and liquid-saturated (LS) Nafion at T = 300 K, for calibration and technique validation, and (b) corresponding calculated water-content profiles. L^* is the normalized sample thickness. The equilibrium times for the membranes are 24 h for the dry one, and 48 h for VS and LS ones (see Supporting Information).

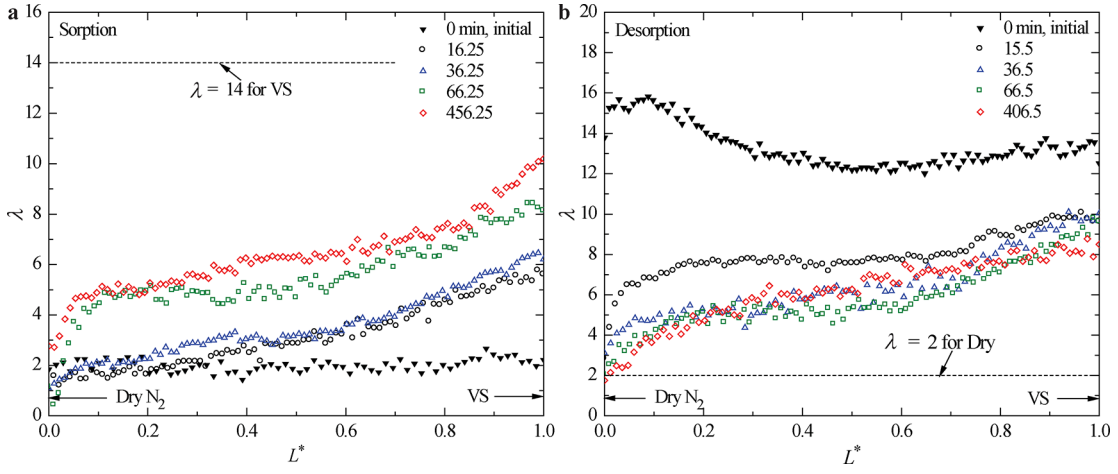

Figure 2. (a) Local water distribution under the dry/vapor-saturated (VS) boundaries for 16.5 to 456.25 min (starting from the dry membrane) and (b) various desorption times for 15.5 to 406.5 min (starting from a VS membrane) at T = 300 K; the initial water-content distribution and the dry and VS N_2 boundaries are also marked. The thicknesses of the membranes are 120, 122, 126, and 122 μm for 16.25, 36.25, 66.25, and 456.25 min sorption times, respectively, and 113, 127, 125, and 111 μm for 15.5, 36.5, 66.5, and 406.5 min desorption times, respectively. Note that the measured membrane thickness is smaller than dry Nafion due to some limitations of this technique in measuring the water profile at the interface (see Supporting Information).

respectively) as a function of normalized membrane thickness, $L^* = x/l$, where l is the membrane thickness. The linear absorption coefficient of the LS sample is lower than that of the dry one due to the lower density of the LS one and lower mass-attenuation coefficient of water compared to Nafion. The raw signals are translated into the water content, λ, as shown Figure 1b, where the dry case is taken to be λ = 2, which is consistent with drying in nitrogen at ambient conditions and is not necessarily the value under perfectly dry conditions.[20] These profiles demonstrate a feasibility to probe the water profile with a high spatial resolution of 1.3 μm per pixel. Note that the significant water uptake difference between the VS and LS ones exhibits Schröder's paradox,[17] as discussed below.

The water profiles during vapor sorption/desorption are shown in Figure 2. In Figure 2a, the water profile was created using dry and VS, that is, 100% relative-humidity (RH) gas-flow boundaries. The designated time represents the time of sorption/desorption plus half of the X-ray imaging time, 5.5 or 6.25 min, depending on the experiment. For sorption, λ gradually increases with the sorption time while the dry side equilibrates with the dry N_2 flow. For 66.25 min sorption, the water profile shows a plateau near $\lambda \sim 5$ (for $0.1 < L^* < 0.6$), implying a large transport coefficient (see the peaks in Figure S4 for further analysis), which is consistent with the maximum diffusivity observed at λ = 3 to 5 in both steady-state[23,24] and dynamic[8,15] measurements. The origin of the fast transport can be explained by two different sorption and transport mechanisms, for example, transition from monolayer water adsorption to capillary in the hydrophilic domains for the bulk-like water behavior[10,25−27] or perhaps by a hydration-dependent, optimal percolation channel for fast transport. This plateau region disappears when the sorption time is long (steady state ~456.25 min), which is associated with the well-distributed percolation channel from the long-term structural rearrangement of the water-induced viscoelastic polymer relaxation.[14] At steady state, the water content near the VS side is lower than expected, that is, less than λ = 14 (see Figure 1). This discrepancy indicates that an interfacial transport resistance

dx.doi.org/10.1021/mz300651a | ACS Macro Lett. 2013, 2, 288−291

exists, which is attributed to a surface morphology wherein the hydrophilic domains are orientated inward due to the preferential alignment of the hydrophobic backbone.[25,28] The transport resistance is not thought to be due to mass transport through a boundary layer (due to the external gas flow), since high flow rates and impinging flow are used,[15] and increasing the flow rate demonstrated no significant change in the profile (see Supporting Information). Here, the interfacial resistance represents the surface-morphology-associated water-transport resistance. A similar resistance phenomenon is also observed at the dry side.

For desorption (Figure 2b), the membrane remains well hydrated at short times, ~15.5 min, having a plateau region near $\lambda \sim 7.5$, while the VS boundary quickly reaches the steady-state value of $\lambda \sim 10$. For longer times, the water content decreases, and the plateau region shifts to $\lambda \sim 5$ at $t = 66.5$ min, similar to that observed in water sorption. At steady state, the water transport coefficient seemingly increases nonlinearly with increasing water content (see Figure S4), which is consistent with water molecules being confined at low hydration to the hydrophilic sulfonic-acid sites, and upon hydration they become more loosely bound, ultimately exhibiting bulk-like behavior.[26,27,29] The steady-state water profile for sorption is consistent with that for desorption, with both demonstrating long times to reach steady state.

A comparison of the short-time and steady-state profiles also demonstrates a change in the slope or concavity in the profile's central region. This change and the associated dependence of the transport coefficients on water content links the dynamic and steady-state ex-situ analyses in the literature by exhibiting a continuous transition from a coefficient that decreases with water content (dynamic due to polymer swelling) and one that increases with water content (steady state).[8] To the authors' knowledge, this is the first time such a transition has been visualized, which provides insights to explain discrepancies in the literature. Because the water-profile transition for short sorption times is in a similar order of temporal resolution, the transient behavior is not unambiguous. In addition, early time transient water profiles, as determined using in-plane small-angle X-ray scattering (SAXS) at multiple points, also exhibit a concave profile or transport coefficient that decreases with water content (see Figure S6), which is different than that obtained from steady-state profiles. This consistency suggests that the results from X-ray tomography technique is free of effects controlling the transport at higher scales as SAXS probes water domain growth at nanoscales.

To investigate the issue of Schröder's paradox (as seen in Figure 1) under a gradient, one boundary was subjected to either dry or humidified gas while the other was in contact with liquid water. Figure 3 shows the desorption profiles for liquid and dry boundaries. Compared to the VS case (Figure 2), a LS boundary demonstrates much shorter times to reach steady state, on the order of 15 min, and with no interfacial resistance on the liquid side. This large difference is consistent with the previous observation of fast liquid-water-driven morphological changes in a LS versus VS reservoir.[30] Thus, the contact with liquid quickly alters the surface morphology to allow water uptake, thus leading to shorter equilibrium time to reach the steady-state water profile.[30] Interestingly, the profiles do not exhibit an abrupt change between $\lambda = 14$ and 22, which might be expected based on previous models and the vast difference between LS and VS water uptake and transport properties.[28] The observed continuous, gradual change exhibited by the

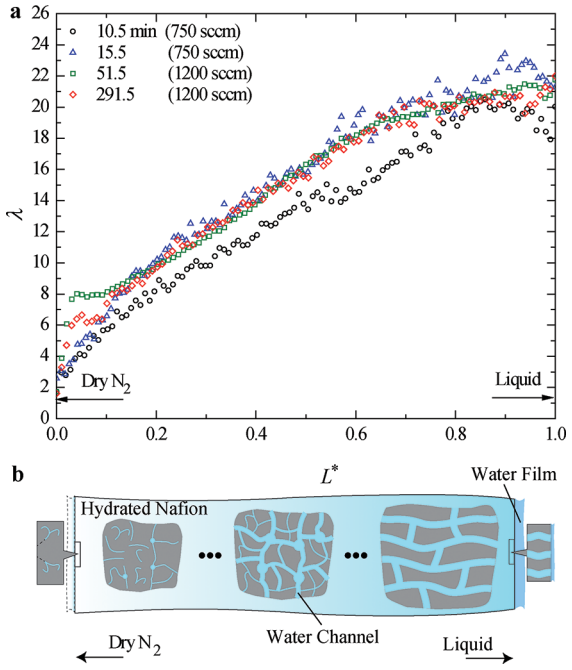

Figure 3. (a) Local water-content profile of Nafion in contact with dry N_2 and liquid water as a function of time. (b) Cartoon of the possible hydrophilic-domain morphologies throughout the hydrated Nafion.

water profiles demonstrates definitive results that an abrupt water-uptake jump does not occur within the membrane for these conditions; the origin of this may be related to the gradual water-capillary/polymer-elastic force balance (speculated from previous studies).[27,28] The results also demonstrate that the fast equilibrium from the liquid water may dominate the transport mechanism, which is also supported by the relatively flat profile (i.e., fast transport) near the LS boundary, which may be related to a penetration depth of the liquid water.[20] Flat profiles around $\lambda = 6$ and 8 for 51.5 and 291.5 min are also found, similar, albeit smaller (especially with the larger axis values in Figure 3), than those seen in the dry/VS boundaries (Figure 2). Analyzing the data in terms of looking at the point-wise slope change in the profile yields a predicted diffusion coefficient (Figure S4) that monotonically increases with increasing hydration except for a deflection point at $10 < \lambda < 16$. This change may be related to a continuous domain-network transition among cylidrical-like or ribbon to clusters or spherical morphologies under water transport from liquid to dry reservoirs (Figure 3b).

From the discussions above, possible qualitative morphological changes with degree of hydration are illustrated in Figure 3b. For low hydration ($\lambda < 5$), the hydrophilic domains are isolated without significant transport channels, which are connected to form a percolated network at moderate hydration ($\lambda \sim 5$). At high hydration, the channels further develop to open transport pathways with reduced tortuosity. At the dry interface, the lack of water and the membrane/environment interactions close the surface transport channels result in a more hydrophobic-like interface and increased interfacial resistance.[31] For the liquid interface, interfacial resistance is not seen and the sulfonic-acid moieties are on the surface, allowing for easy water ingress.

To explore Schröder's paradox and related transport in more detail, the water profiles for LS and VS boundaries are shown in Figure 4. Regardless of experiment time and hydration

dx.doi.org/10.1021/mz300651a | ACS Macro Lett. 2013, 2, 288−291

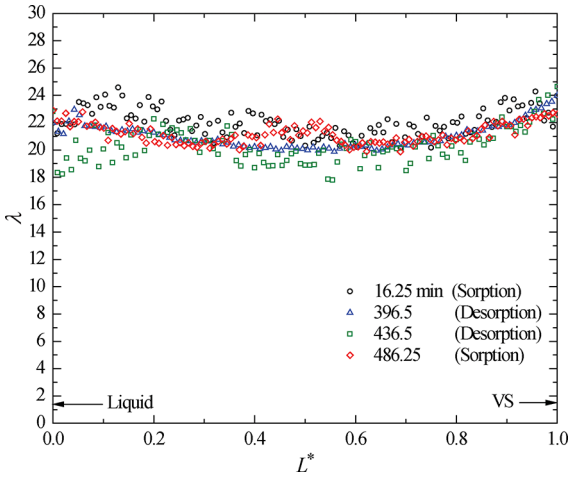

Figure 4. Local membrane water-content profile in contact with vapor-saturated (VS) N_2 and liquid water for both sorption and desorption over the times of 16.25, 396.5, 436.5, and 486.25 min.

pathways, the membranes are uniformly LS throughout. This explains that the hydration kinetics and morphological rearrangement (both within membrane and at the surface) from liquid are much faster than those from vapor. The flat profile suggests that there is water transport from the liquid to the vapor boundary under the same nominal chemical potential of the outside reservoirs. A liquid film could also possibly form on the VS boundary due to the partially hydrophilic nature of the membrane surface. However, with a reduced RH at the VS side (i.e., 90%), the same profiles were obtained (Figure S5), implying that the contribution from possible vapor condensation is minor and that it is dominated by the water transport across the membrane from the liquid side.

In summary, the technique described here was used to investigate water transport through Nafion with relatively high spatial and temporal resolutions. The obtained results help to resolve critical, long-lasting debates, such as (a) the much faster and gradual, continuous profile without dramatic water-uptake change between λ = 14 and 22 (or VS and LS), (b) the existence of uniform profile (λ = 22) with LS/VS boundaries, (c) the dominance of interfacial resistance for dry vapor boundaries, and (d) the highly nonlinear water profile with a transition from expected transient to steady state including possible transport mechanism and dependence changes. The findings provide a firm foundation for the rational material design for the desired functionalities and operations of Nafion and related ionomers. In addition, the developed visualization technique can also be employed to articulate the characteristic penetrant behaviors of crucial polymers, nanocomposites, or macromolecular materials for their optimal design.

■ ASSOCIATED CONTENT

Ⓢ Supporting Information

Detailed experimental procedures, literature survey, and data analysis. This material is available free of charge via the Internet at http://pubs.acs.org.

■ AUTHOR INFORMATION

Corresponding Author

*E-mail: azweber@lbl.gov. Phone: +1-510-486-6308.

Notes

The authors declare no competing financial interest.

■ ACKNOWLEDGMENTS

This work was supported by the Assistant Secretary for Energy Efficiency and Renewable Energy, Fuel Cell Technologies Office, of the U.S. DOE under Contract No. DE-AC02-05CH11231. Computed X-ray tomography were carried out at the Advanced Light Source, which is supported by the Director, Office of Science, of the U.S. DOE under the same contract. We also thank Kurt Krueger for machining the sample holder.

■ REFERENCES

(1) Li, J.; Park, J. K.; Moore, R. B.; Madsen, L. A. *Nat. Mater.* **2011**, *10*, 507.
(2) Schmidt-Rohr, K.; Chen, Q. *Nat. Mater.* **2008**, *7*, 75.
(3) Kreuer, K. D.; Paddison, S. J.; Spohr, E.; Schuster, M. *Chem. Rev.* **2004**, *104*, 4637.
(4) Weber, A. Z.; Mench, M. M.; Meyers, J. P.; Ross, P. N.; Gostick, J. T.; Liu, Q. H. *J. Appl. Electrochem.* **2011**, *41*, 1137.
(5) Hickner, M. A. *J. Polym. Sci., Part B: Polym. Phys.* **2012**, *50*, 9.
(6) Mauritz, K. A.; Moore, R. B. *Chem. Rev.* **2004**, *104*, 4535.
(7) Hickner, M. A. *Mater. Today* **2010**, *13*, 34.
(8) Kusoglu, A.; Weber, A. Z. *Polymers for Energy Storage and Delivery: Polyelectrolytes for Batteries and Fuel Cells*; American Chemical Society: Washington, DC, 2012; Vol. *1096*, p 175.
(9) Deabate, S.; Gebel, G.; Huguet, H.; Morin, A.; Pourcelly, G. *Energy Environ. Sci.* **2012**, *5*, 8824.
(10) Zawodzinski, T. A.; Derouin, C.; Radzinski, S.; Sherman, R. J.; Smith, V. T.; Springer, T. E.; Gottesfeld, S. *J. Electrochem. Soc.* **1993**, *140*, 1041.
(11) Kim, M.-H.; Glinka, C. J.; Grot, S. A.; Grot, W. G. *Macromolecules* **2006**, *39*, 4775.
(12) Motupally, S.; Becker, A. J.; Weidner, J. W. *J. Electrochem. Soc.* **2000**, *147*, 3171.
(13) Pivovar, A. M.; Pivovar, B. S. *J. Phys. Chem. B* **2005**, *109*, 785.
(14) Hallinan, D. T.; De Angelis, M. G.; Giacinti Baschetti, M.; Sarti, G. C.; Elabd, Y. A. *Macromolecules* **2010**, *43*, 4667.
(15) Hallinan, D. T.; Elabd, Y. A. *J. Phys. Chem. B* **2009**, *113*, 4257.
(16) Satterfield, M. B.; Benziger, J. B. *J. Phys. Chem. B* **2008**, *112*, 3693.
(17) Schroeder, P. *Z. Phys. Chem.* **1903**, *45*, 57.
(18) Freger, V. *J. Phys. Chem. B* **2009**, *113*, 24.
(19) Onishi, L. M.; Prausnitz, J. M.; Newman, J. *J. Phys. Chem. B* **2007**, *111*, 10166.
(20) Hussey, D. S.; Hussey, D. S.; Spernjak, D.; Weber, A. Z.; Mukundan, R.; Fairweather, J.; Brosha, E. L.; Davey, J.; Spendelow, J. S.; Jacobson, D. L.; Borup, R. L. *J. Appl. Phys.* **2012**, *112*, 104906.
(21) Kientiz, B. a. G., J. and MacDowell, A. and Weber, A. Z. In 218th Electrochemical Society Meeting, Las Vegas, Nevada, October 10−15, 2010, The Electrochemical Society: Pennington, NJ, 2010.
(22) Albertini, V. R.; Paci, B.; Nobili, F.; Marassi, R.; Michiel, M. D. *Adv. Mater.* **2009**, *21*, 578.
(23) Zawodzinski, T. A.; Neeman, M.; Sillerud, L. O.; Gottesfeld, S. *J. Phys. Chem.* **1991**, *95*, 6040.
(24) Mittelsteadt, C. K.; Staser, J. *ECS Trans.* **2011**, *41*, 101.
(25) Zhao, Q. A.; Majsztrik, P.; Benziger, J. *J. Phys. Chem. B* **2011**, *115*, 2717.
(26) Hwang, G. S.; Kaviany, M.; Gostick, J. T.; Kientiz, B.; Weber, A. Z.; Kim, M. H. *Polymer* **2011**, *52*, 2584.
(27) Kreuer, K. D. *Solid State Ionics* **2000**, *136*, 149.
(28) Kientiz, B.; Yamada, H.; Nonoyama, N.; Weber, A. Z. *J. Fuel Cell Sci. Technol.* **2011**, *8*, 064501.
(29) Kornyshev, A. A.; Kuznetsov, A. M.; Spohr, E.; Ulstrup, J. *J. Phys. Chem. B* **2003**, *107*, 3351.
(30) Kusoglu, A.; Modestino, M. A.; Hexemer, A.; Segalman, R. A.; Weber, A. Z. *ACS Macro Lett.* **2012**, *1*, 33.
(31) He, Q. G.; Kusoglu, A.; Lucas, I. T.; Clark, K.; Weber, A. Z.; Kostecki, R. *J. Phys. Chem. B* **2011**, *115*, 11650.